

# The hadronic vacuum polarization contribution to $a_\mu$ from full lattice QCD

Bipasha Chakraborty,<sup>1</sup> C. T. H. Davies,<sup>1,\*</sup> P. G. de Oliveira,<sup>1</sup> J. Koponen,<sup>1</sup> and G. P. Lepage<sup>2</sup>  
(HPQCD collaboration),<sup>†</sup>

R. S. Van de Water<sup>3</sup>

<sup>1</sup>*SUPA, School of Physics and Astronomy, University of Glasgow, Glasgow, G12 8QQ, UK*

<sup>2</sup>*Laboratory for Elementary-Particle Physics, Cornell University, Ithaca, New York 14853, USA*

<sup>3</sup>*Fermi National Accelerator Laboratory, Batavia, IL, USA*

(Dated: May 30, 2017)

We determine the contribution to the anomalous magnetic moment of the muon from the  $\alpha_{\text{QED}}^2$  hadronic vacuum polarization diagram using full lattice QCD and including  $u/d$  quarks with physical masses for the first time. We use gluon field configurations that include  $u$ ,  $d$ ,  $s$  and  $c$  quarks in the sea at multiple values of the lattice spacing, multiple  $u/d$  masses and multiple volumes that allow us to include an analysis of finite-volume effects. We obtain a result for  $a_\mu^{\text{HVP,LO}}$  of  $667(6)(12) \times 10^{-10}$ , where the first error is from the lattice calculation and the second includes systematic errors from missing QED and isospin-breaking effects and from quark-line disconnected diagrams. Our result implies a discrepancy between the experimental determination of  $a_\mu$  and the Standard Model of  $3\sigma$ .

## I. INTRODUCTION

The muon's gyromagnetic ratio  $g_\mu$  is known experimentally with extremely high accuracy: its magnetic anomaly,  $a_\mu \equiv (g_\mu - 2)/2$ , has been measured to 0.5 ppm [1] and a new experiment aims to reduce that uncertainty to 0.14 ppm [2]. By comparing these results with Standard Model predictions, we can use the muon's anomaly to search for indirect evidence of new physics beyond the mass range directly accessible at the Large Hadron Collider. There are tantalizing hints of a discrepancy between theory and experiment—the difference is currently 2.2(7) ppm [3]—but more precision is needed. In particular the Standard Model prediction, which currently is known to about 0.4 ppm [3], must be substantially improved in order to match the expected improvement from experiment.

The largest theoretical uncertainty in  $a_\mu$  comes from the vacuum polarization of hadronic matter (quarks and gluons) as illustrated in Figure 1. This contribution has been estimated to a little better than 1% (which is 0.6 ppm of  $a_\mu$ ) from experimental data on  $e^+e^- \rightarrow$  hadrons and  $\tau$  decay [4–8], but much recent work [9–18] has focused on a completely different approach, using Monte Carlo simulations of lattice QCD [19], which promises to deliver smaller errors in the future.

In an earlier paper [14], we introduced a new technique for the lattice QCD analyses that allowed us to calculate the  $s$  quark's vacuum-polarization contribution from Figure 1 with a precision of 1% for the first time. Here we extend that analysis to the much more important (and difficult to analyze) case of  $u$  and  $d$  quarks, allowing us to obtain the complete contribution from hadronic vacuum

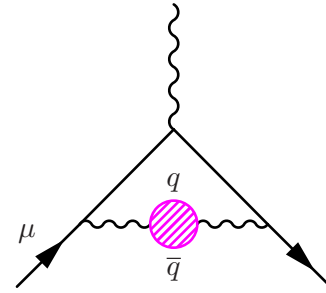


FIG. 1: The  $\alpha_{\text{QED}}^2$  hadronic vacuum polarization contribution to the muon anomalous magnetic moment is represented as a shaded blob inserted into the photon propagator (represented by a wavy line) that corrects the point-like photon-muon coupling at the top of the diagram.

polarization at  $\alpha_{\text{QED}}^2$ . We achieve a precision of 2%, for the first time from lattice QCD. A large part of our uncertainty is from QED, isospin breaking and quark-line disconnected effects that were not included in the simulations, but will be in future simulations. The remaining systematic errors add up to only 1%. A detailed analysis of these systematic errors allows us to map out a strategy for reducing lattice QCD errors well below 1% using computing resources that are substantial but currently available.

## II. LATTICE QCD CALCULATION

Almost all of the hadronic vacuum polarization contribution (HVP) comes from *connected* diagrams with the structure shown in Figure 1: the photon creates a quark and antiquark which propagate, while interacting with each other, and eventually annihilate back into a photon. Here we analyze the case where the photon creates

\*christine.davies@glasgow.ac.uk

†URL: <http://www.physics.gla.ac.uk/HPQCD>

TABLE I: Here we use gluon field configurations from the MILC collaboration [20, 21].  $\beta = 10/g^2$  is the QCD gauge coupling, and  $w_0/a$  [22] gives the lattice spacing,  $a$ , in terms of the Wilson flow parameter,  $w_0$  [23]. We take  $w_0=0.1715(9)$  fm fixed from  $f_\pi$  [22]. The lattice spacings are approximately 0.15 fm for sets 1–3, 0.12 fm for sets 4–8, and 0.09 fm for sets 9–10.  $L$  and  $T$  are the spatial and temporal dimensions of the lattice.  $am_\ell, am_s$  and  $am_c$  are the masses in lattice units of light ( $m_\ell \equiv m_u = m_d$ ), strange, and charm quarks in the sea, with  $am_s^{\text{phys}}$  giving the correct  $m_s$  value on that ensemble [24]. Valence quark masses equal  $m_\ell$  except for set 4, where  $am_\ell^{\text{val}} = 0.01044$  is slightly different from  $am_\ell$ .  $am_\pi$  and  $am_\rho$  give the corresponding masses for the  $\pi$  and  $\rho$  mesons;  $f_\rho$  is the lattice result for the  $\rho$ 's leptonic decay constant.  $Z_{V,\bar{s}s}$  gives the vector current renormalization factor (calculated for  $s$  quarks) obtained nonperturbatively [25]. The number of configurations is given in the final column; we use 16 time sources on each and average over the spatial polarizations for the vector current. We tested for autocorrelations by binning configurations, but found no effect.

Set	$\beta$	$w_0/a$	$am_\ell$	$am_s$	$am_c$	$am_s^{\text{phys}}$	$am_\pi$	$am_\rho$	$f_\rho/(m_\rho Z_{V,\bar{s}s})$	$Z_{V,\bar{s}s}$	$L/a \times T/a$	$n_{\text{cfg}}$
1	5.8	1.1119(10)	0.013	0.065	0.838	0.0700(9)	0.23643(9)	0.6679(15)	0.2659(9)	0.9887(20)	$16 \times 48$	9947
2	5.8	1.1272(7)	0.0064	0.064	0.828	0.0686(8)	0.16617(7)	0.6128(47)	0.2677(19)	0.9887(20)	$24 \times 48$	1000
3	5.8	1.1367(5)	0.00235	0.0647	0.831	0.0677(8)	0.10172(4)	0.5968(45)	0.2776(16)	0.9887(20)	$32 \times 48$	997
4	6.0	1.3826(11)	0.0102	0.0509	0.635	0.0545(7)	0.18938(8)	0.5276(35)	0.2635(23)	0.9938(17)	$24 \times 64$	1053
5	6.0	1.4029(9)	0.00507	0.0507	0.628	0.0533(7)	0.13492(8)	0.4938(82)	0.2625(63)	0.9938(17)	$24 \times 64$	1020
6	6.0	1.4029(9)	0.00507	0.0507	0.628	0.0533(7)	0.13415(5)	0.4866(49)	0.2635(34)	0.9938(17)	$32 \times 64$	1000
7	6.0	1.4029(9)	0.00507	0.0507	0.628	0.0534(7)	0.13401(6)	0.4850(46)	0.2652(31)	0.9938(17)	$40 \times 64$	331
8	6.0	1.4149(6)	0.00184	0.0507	0.628	0.0527(6)	0.08162(4)	0.4730(27)	0.2771(11)	0.9938(17)	$48 \times 64$	998
9	6.3	1.9006(20)	0.0074	0.037	0.44	0.0378(5)	0.14062(10)	0.3854(37)	0.2626(29)	0.9944(10)	$32 \times 96$	1000
10	6.3	1.9330(20)	0.00363	0.0363	0.43	0.0366(5)	0.09850(10)	0.3508(42)	0.2683(33)	0.9944(10)	$48 \times 96$	298

either a  $u\bar{u}$  or  $d\bar{d}$  pair; we calculated contributions from heavier quarks in [14, 26, 27]. Disconnected diagrams, where the quarks and antiquarks created by the photons annihilate into gluons rather than photons, give much smaller contributions [28, 29]; we will discuss these at the end of this paper.

In Section II A, we describe how we extract  $a_\mu$  from a single configuration set. Unlike in our previous analysis with  $s$  quarks [14], the light-quark vacuum polarization becomes very noisy at large  $t$  for physical masses. We introduce a simple procedure for improving the signal-to-noise ratio in this calculation.

In Section II B, we examine the largest systematic errors in our lattice analysis. These come from finite-volume effects, and, more importantly, from mass splittings between different tastes of pion in our HISQ formalism. We address these errors in two ways.

First we use chiral perturbation theory to calculate corrections, including contributions from the leading term and the largest corrections to it. We also calculate contributions from a variety of other higher-order corrections in order to assess their impact on  $a_\mu$ .

The second way in which we address our systematic errors is to extract values for  $a_\mu$  from simulations with much larger light-quark masses — approximately 2.5 and 5 times the physical mass — where systematic errors from finite volumes and staggered pions become negligible. As discussed in [13], most of the light-quark mass dependence of  $a_\mu$  can be removed by rescaling the vacuum polarization with appropriate powers of  $m_\rho^{\text{latt}}/m_\rho^{\text{expt}}$ . Here we show that rescaled results from large masses are consistent with the corrected results from physical masses, giving us confidence in both types of result. We combine all of our results into a single global fit from which we extract a final result.

## A. Extracting $a_\mu$

The leading-order contribution to the muon anomalous magnetic moment from the HVP is obtained by inserting the quark vacuum polarization into the photon propagator [30, 31]. Ignoring disconnected contributions, the vacuum polarization separates into distinct contributions for each quark flavour,  $f$ :

$$a_\mu^{\text{HVP,LO}}(f) = \frac{\alpha}{\pi} \int_0^\infty dk^2 f(k^2) (4\pi\alpha) \hat{\Pi}_f(k^2) \quad (1)$$

where  $\alpha \equiv \alpha_{\text{QED}}$  is the QED fine structure constant and  $k$  is the (Euclidean) momentum carried by the virtual photons.  $f(k^2)$  is a kinematic factor that diverges as  $k^2 \rightarrow 0$ , where the renormalized vacuum polarization function,  $\hat{\Pi}(k^2) \equiv \Pi(k^2) - \Pi(0)$ , vanishes. The resulting integrand is peaked around  $k^2 \approx m_\mu^2$ . Note that  $\hat{\Pi}(k^2)$  includes a factor of  $Q_f^2$ , where  $Q_f$  is the electric charge of quark  $f$  in units of the proton's charge. This is a change to the convention that we used in [14].

Lattice QCD is used to calculate the vacuum polarization function  $\hat{\Pi}(k^2)$ . In [14] we developed an accurate method for evaluating Eq. (1) by defining  $\hat{\Pi}(k^2)$  in terms of its Taylor expansion,

$$\hat{\Pi}(k^2) = \sum_{j=1}^{\infty} k^{2j} \Pi_j, \quad (2)$$

where the Taylor coefficients  $\Pi_j$  are determined from time-moments  $G_{2j}$  of the vector current-current corre-

lator at zero spatial momentum:

$$\begin{aligned}
G_{2j} &\equiv \sum_t \sum_{\vec{x}} t^{2j} Z_V^2 \langle j^i(\vec{x}, t) j^i(0) \rangle \\
Q_f^2 G_{2j} &= (-1)^j \left. \frac{\partial^{2j}}{\partial k^{2j}} k^2 \hat{\Pi}(k^2) \right|_{k^2=0} \\
&= (-1)^j (2j)! \Pi_{j-1}. \tag{3}
\end{aligned}$$

Here  $Z_V$  renormalizes the lattice vector current, and

$$t \in (0, 1, 2, \dots, T/2 - 1, 0, -T/2 + 1, \dots, -2, -1). \tag{4}$$

We replace the Taylor series by its  $[n, n]$  and  $[n, n-1]$  Padé approximants for the integral in Eq. (1). The approximants provide an accurate approximation for both the low and high  $k^2$  regions in the integral, and results converge to better than 1% by  $n = 2$ , with the exact result bracketed by results from the  $[n, n]$  and  $[n, n-1]$  approximants for each  $n$  [14]. We evaluate the integral numerically.

Signal/noise in lattice QCD (Monte Carlo) evaluations of vector correlators degrades exponentially as the time separation,  $t$ , between source and sink increases. This increases the uncertainties in the  $\Pi_j$  from Eq.(3), especially as  $j$  increases. The noise problem is particularly acute for correlators made of  $u/d$  quarks, because the  $\rho$  (which controls the signal) is much more massive than the  $\pi$  (which controls the noise) [32]. The values that a correlator can take at large  $t$ , however, are constrained by its values at smaller  $t$  and the known form of the correlator. Thus we reduce the noise in our Taylor coefficients by replacing the correlator at large- $t$  with its value determined from a standard multi-exponential fit (to data at all  $ts$ , large and small). We use

$$G(t) = \begin{cases} G_{\text{data}}(t), & t \leq t^* \\ G_{\text{fit}}(t), & t > t^* \end{cases}. \tag{5}$$

and test that our results are stable on varying  $t^*$ . We find  $a_\mu$  to be independent of  $t^*$  to better than  $\pm 0.5\%$  for  $t^*$  values ranging between 0.5 fm and 1.5 fm (our default value since larger values lead to larger statistical errors). To further improve our results, we calculate a  $2 \times 2$  matrix of vector correlators that combines the local operator we need for the time-moments (Eq. (3)) with a smeared operator that overlaps more strongly with the ground-state vector meson (the  $\rho$ ). Using the fit at large  $t$  also allows us to correct for the finite temporal length of the lattice.

We present more details on this noise-reduction strategy in Appendix A. There we show that this strategy introduces a new uncertainty into our analysis, due to low-energy ( $< m_\rho$ )  $\pi\pi$  states in the simulations. We estimate this uncertainty using chiral perturbation theory. We also show that the uncertainty is bounded by the variation of  $a_\mu$  as  $t^*$  is changed from 0.5 fm to 1.5 fm. Our estimate is consistent with the variation in  $a_\mu$  mentioned above, so we include an uncertainty of  $\pm 0.5\%$  in our error budget to allow for these effects.

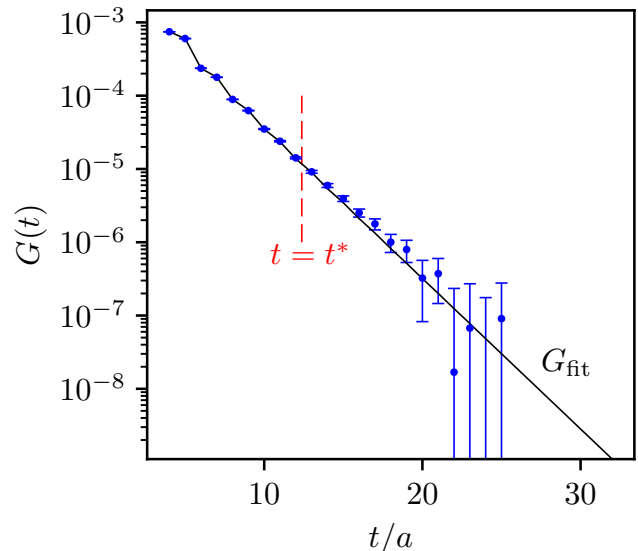


FIG. 2: Monte Carlo data for the current-current correlator on configuration set 8 from Table II compared with the fit function  $G_{\text{fit}}$  that replaces the data for  $t > t^*$ .  $G_{\text{fit}}$  is obtained from a multi-exponential fit to all the data shown, above and below  $t^*$ , together with additional data for correlators with smeared sources. Its uncertainty is of order the width of the line at large  $t$ , and smaller at small  $t$ . The oscillations at small  $t$  are an artifact of staggered quarks whose contribution to  $a_\mu$  is small and vanishes with the lattice spacing.

We work on ensembles of gluon field configurations that have an improved discretization of the gluon action [33] and sea  $u$ ,  $d$ ,  $s$ , and  $c$  quarks using the Highly Improved Staggered Quark (HISQ) action [34, 35]. They were generated by the MILC collaboration [21]. We have results for three lattice spacings, for  $u/d$  quark masses ranging from  $m_s/5$  down to the physical value, and for three lattice volumes, for one combination of masses and lattice spacing. These results allow us to test and correct for the most important systematic errors in our simulations. We approximate  $m_u = m_d \equiv m_\ell$ , using the same masses for valence and sea quarks. The ensembles are described in Table I.

A by-product of the fits to our lattice QCD correlators are values for the  $\rho$  mass and decay constant for a variety of  $u/d$  quark masses. Our results agree with experiment to within errors for realistic quark masses (see Appendix A). This is an important test of the correlators we use to calculate  $a_\mu^{\text{HVP,LO}}$ .

The local vector current that we use is not the conserved vector current for this quark action and so must be renormalized. We do this nonperturbatively by demanding that the vector form factor for this current be 1 between two equal mass mesons at rest ( $q^2 = 0$ ) [25]. We use pseudoscalar mesons made of  $s$  quarks to do this, on the  $m_\ell/m_s=0.2$  ensembles at each lattice spacing and give values in Table I. We ignore the mass dependence of

TABLE II: Columns 2-5 give the uncorrected Taylor coefficients  $\Pi_j$  (Eq. 2), in units of  $1/\text{GeV}^{2j}$ , for each of the lattice data sets in Table I. The errors given include statistics and the (correlated) uncertainty from setting the lattice spacing using  $w_0$ ; the latter error largely cancels in our analysis. Estimates of the connected contribution from  $ud$ -quarks to  $a_\mu^{\text{HVP,LO}}$  are given for each of the  $[1, 0]$ ,  $[1, 1]$ ,  $[2, 1]$  and  $[2, 2]$  Padé approximants in columns 6-9; results are multiplied by  $10^{10}$ . These estimates are obtained after correcting the moments, as discussed in the text. The final estimate for  $a_\mu^{\text{HVP,LO}}$  is given in the last column.

Set	$\Pi_1$	$\Pi_2$	$\Pi_3$	$\Pi_4$	$[1, 0] \times 10^{10}$	$[1, 1] \times 10^{10}$	$[2, 1] \times 10^{10}$	$[2, 2] \times 10^{10}$	$a_\mu^{\text{HVP,LO}} \times 10^{10}$
1	0.0624 (7)	-0.0760(17)	0.102 (3)	-0.138 (6)	660.1 (3.2)	590.7 (2.8)	593.3 (2.9)	592.2 (2.9)	592.7 (3.0)
2	0.0729(11)	-0.1028(31)	0.159 (8)	-0.250(16)	663.8 (6.0)	591.7 (5.2)	595.8 (5.5)	593.6 (5.5)	594.7 (5.6)
3	0.0796(13)	-0.1182(39)	0.190(10)	-0.311(21)	689.9 (9.2)	604.4 (8.9)	618.3 (11.3)	609.1 (10.5)	613.7(11.5)
4	0.0638 (8)	-0.0803(21)	0.111 (5)	-0.157 (9)	650.0 (5.7)	582.5 (4.9)	585.0 (4.9)	584.0 (4.9)	584.5 (4.9)
5	0.0715(13)	-0.0992(41)	0.151(11)	-0.236(24)	653.4 (14.1)	583.4 (11.8)	587.4 (12.0)	585.3 (11.9)	586.4(11.9)
6	0.0736(11)	-0.1052(33)	0.166 (9)	-0.267(19)	650.8 (8.3)	581.5 (7.0)	585.4 (7.2)	583.4 (7.1)	584.4 (7.2)
7	0.0744(11)	-0.1075(34)	0.171 (9)	-0.277(20)	652.9 (7.8)	583.5 (6.6)	587.2 (6.8)	585.2 (6.7)	586.2 (6.8)
8	0.0811(12)	-0.1239(36)	0.206 (9)	-0.345(21)	675.1 (7.6)	593.6 (7.5)	606.9 (9.6)	597.9 (8.9)	602.4(10.0)
9	0.0625 (9)	-0.0778(25)	0.107 (6)	-0.151(11)	640.1 (7.3)	574.2 (6.2)	576.6 (6.2)	575.7 (6.2)	576.2 (6.2)
10	0.0755(13)	-0.1109(41)	0.178(11)	-0.292(25)	652.1 (8.4)	583.4 (7.2)	586.7 (7.3)	585.0 (7.2)	585.8 (7.2)

the  $Z_V$ s since it is less than 0.1% ( $\mathcal{O}((am_s/\pi)^2\alpha_s)$ ) and therefore negligible compared to our statistical errors.

### B. Correcting $a_\mu$

The Taylor coefficients  $\Pi_j$  from each of our  $u/d$ -quark vector correlators are listed in Table II. We introduce two corrections, one after the other, before calculating  $a_\mu^{\text{HVP,LO}}$  in order to minimize our systematic errors:

1. *Reduce lattice artifacts:* We correct our results for errors caused by the finite spatial volume of the lattice and by artifacts from using (HISQ) staggered quarks (mass splittings between pions of different taste). We do this with an effective theory, derived from chiral perturbation theory, that couples  $\rho$ s,  $\pi^+\pi^-$  pairs, and  $\gamma$ s. We use the theory to calculate the  $\Pi_j$  for both the continuum and our lattice QCD calculation, and we correct our lattice QCD moments with the differences. The corrections for each moment and configuration set are given in Table IV of Appendix B3. The largest corrections for  $a_\mu$  are for our lightest pions and turn out to be around +7%. They are an order of magnitude smaller for our heaviest pions. These corrections lead to an uncertainty of  $\pm 0.7\%$  in our final  $a_\mu$ .

Chiral perturbation theory is well suited to our analysis because our moments are calculated at  $q^2 = 0$ , where chiral perturbation theory is valid. The dominant finite-volume and staggered-pion corrections come from leading-order pion vacuum polarization,  $\gamma \rightarrow \pi^+\pi^- \rightarrow \gamma$ , as discussed in [36]. This correction can be calculated quite accurately because it is determined by the (well measured) charge and mass of the pion. We find that it is five times larger than the other corrections. The next largest contribution comes from corrections to the  $\gamma\text{-}\pi\pi$  vertex due to the pion's charge radius. We

include both of these corrections in our final result, together with a variety of the other higher-order corrections that allow us to explore the rate of convergence of chiral perturbation theory. See Appendix B3 for more details.

2. *Reduce  $m_\ell$  dependence:* We rescale  $m_\ell$  to its physical value in the  $\pi\pi$  and  $\rho$  contributions to  $a_\mu$  (80% of the total) to reduce  $a_\mu$ 's strong dependence on  $m_\ell$ . We do this in three steps, modifying and extending a method introduced in [13]:

(a) We remove the vacuum polarization contribution to  $a_\mu$  due to  $\gamma \rightarrow \pi^+\pi^- \rightarrow \gamma$  using the continuum effective field theory with the pion mass set equal to the simulation result for the Goldstone pion.

(b) We rescale the resulting  $\Pi_j$  by  $(m_\rho^{\text{latt}}/m_\rho^{\text{expt}})^{2j}$ . This reduces  $m_\ell$  dependence because the  $\rho$  meson pole dominates the vacuum polarization, especially once the  $\pi^+\pi^-$  contribution is removed. We also find that rescaling removes further finite volume dependence; see the end of Appendix B3. Rescaling has a large impact for our heavier-than-physical  $m_\ell$  values, but has little effect for physical  $m_\ell$  where the simulation's  $m_\rho$  agrees with experiment. We apply the Padé approximants at this stage to generate estimates for  $a_\mu^{\text{HVP,LO}}$ , since they converge more quickly without the  $\pi^+\pi^-$  contribution (which is restored in the next step).

(c) We reintroduce the  $\pi^+\pi^-$  contribution removed in step 2a, but with the pion mass set equal to  $m_{\pi^+}$  (139.6 MeV) rather than the pion masses from the simulations. Again this has little impact for our configurations with physical  $m_\ell$  values.

Our results, using different Padé approximants, are shown in Table II. Our final result for each configuration is obtained by taking a value half way between results from the  $[2, 2]$  and  $[2, 1]$  Padé approximants, with

an associated error equal to half the difference [14]. Our statistics do not permit the use of higher-order approximations.

Our corrected results are plotted in Figure 3, together with the results without corrections (labeled “raw”). The corrected results are nearly independent of  $m_\ell$ , as expected. Residual dependence comes from other hadronic channels in the vacuum polarization beyond the  $\pi^+\pi^-$  and  $\rho$  contributions. The corrected results also show smaller  $a^2$  and volume dependence, as is particularly clear from the points for  $\delta m_\ell/m_s$  just above 0.05.

The final step in our analysis is to fit the corrected results from our 10 ensembles to a function of the form

$$a_\mu^{\text{HVP,LO}} \left( 1 + c_\ell \frac{\delta m_\ell}{\Lambda} + c_s \frac{\delta m_s}{\Lambda} + \tilde{c}_\ell \frac{\delta m_\ell}{m_\ell} + c_{a^2} \frac{(a\Lambda)^2}{\pi^2} \right) \quad (6)$$

where  $\delta m_f \equiv m_f - m_f^{\text{phys}}$ , and  $\Lambda \equiv 5m_s$  is of order the QCD scale (0.5 GeV). The fit parameters have the following priors:

$$c_\ell = 0(1) \quad c_s = 0.0(3) \quad \tilde{c}_\ell = 0.00(3) \quad c_{a^2} = 0(1) \quad (7)$$

together with prior  $600(200) \times 10^{-10}$  for  $a_\mu^{\text{HVP,LO}}$ . This fit corrects for mis-tuned quark masses and the finite lattice spacing. The first two correction terms allow for residual dependence on  $m_\ell$  and (slight) mistuning in the  $s$  quark’s mass. We expect smaller corrections from the latter because it enters only through the quark sea. The last term in Eq. (6) corrects for the finite-lattice spacing. Note that our analysis is quite insensitive to uncertainties in the lattice spacing because the leading dependence on the lattice spacing cancels when we rescale our moments with the lattice result for the rho mass (step 2 in our analysis).

The  $\delta m_\ell/m_\ell$  correction in Eq. (6) is associated with steps 2(a) and 2(c) in our analysis, where we replace the (continuum)  $\gamma \rightarrow \pi\pi \rightarrow \gamma$  contribution to  $a_\mu$  corresponding to the simulation’s pion mass with the same contribution evaluated at the physical pion mass. The  $\Pi_1$  Taylor coefficient dominates  $a_\mu$  (see the [1, 0] entries in Table II) and therefore Eq. (B25) in Appendix B implies that  $a_\mu$ ’s dependence on the light-quark mass  $m_\ell$  is given approximately by

$$a_\mu(m_\ell) \approx a_0 \left( 1 + d_\ell \frac{m_\ell^{\text{phys}}}{m_\ell} \right) \quad (8)$$

where  $a_0$  and  $d_\ell$  depend weakly on  $m_\ell$ ,  $m_\ell^{\text{phys}}$  is the physical value for  $m_\ell$ , and the physical value for  $a_\mu$  is approximately  $a_0(1 + d_\ell)$ . The bulk of the  $d_\ell$  term comes from  $\gamma \rightarrow \pi\pi \rightarrow \gamma$  vacuum polarization, with  $d_\ell \approx 0.1$ . So steps 2(a) and 2(c) in our analysis procedure have the effect of replacing  $m_\ell$  by  $m_\ell^{\text{phys}}$ , thereby bringing  $a_\mu(m_\ell)$  closer to its physical value. About a quarter of  $d_\ell$  comes from sources other than the simple  $\pi\pi$  vacuum polarization—the most important is from  $\gamma \rightarrow \rho \rightarrow \pi\pi \rightarrow \gamma$ .

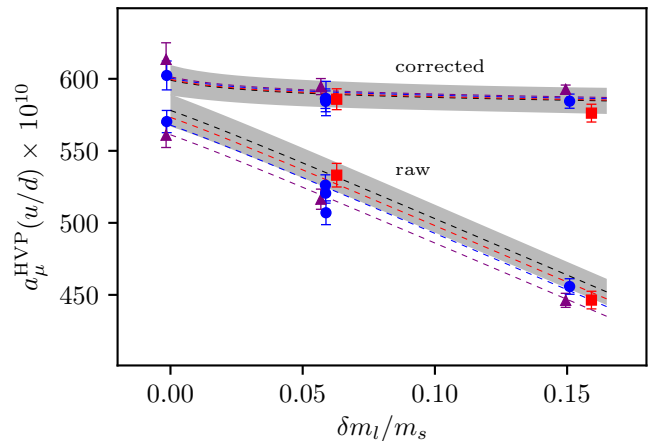


FIG. 3: Our results for the connected  $u/d$  contribution to  $a_\mu^{\text{HVP,LO}}$  as a function of the  $u/d$  quark mass (expressed as its deviation from the physical value in units of the physical  $s$  quark mass). The lower curve shows our uncorrected data; the upper curve includes correction factors discussed in the text and is used to obtain the final result. Data come from simulations with lattice spacings of 0.15 fm (purple triangles), 0.12 fm (blue circles), and 0.09 fm (red squares). The gray bands show the  $\pm 1\sigma$  predictions of our model (Eq. (7)) after fitting it to the data. The dashed lines show the results from the fitting function for each lattice spacing (colored as above) and extrapolated to zero lattice spacing (black). The  $\chi^2$  per degree of freedom was 1.0 and 0.6 for the upper and lower fits, respectively.

Thus our analysis steps 2(a) and 2(c) do not fully correct the  $m_\ell$  in Eq. (8). There is a residual piece of order  $a_0 \times 0.2 d_\ell \delta m_\ell/m_\ell$  that we account for with the  $\delta m_\ell/m_\ell$  correction in our fit formula. In practice the contribution from this term is comparable to our statistical errors, and so has marginal impact on our final result.

We tested our fit by adding higher-order terms in the various corrections and cross terms. None of these variations changed our final results by more than a small fraction of the final uncertainty.

We also tested our fit by dropping various configuration sets. Dropping the configuration sets with the heaviest pions (sets 1, 4 and 9) shifts our final result for  $a_\mu$  by less than a fifth of a standard deviation and leaves the total error unchanged. Dropping the sets with physical pion masses (sets 3 and 8) shifts the final result by a standard deviation and increases the final error by 30%. Each variation is consistent, within errors, with the full analysis.

Our final result from the fit for the connected contribution from  $u/d$  quarks is  $a_\mu^{\text{HVP,LO}} = 599(6)(8) \times 10^{-10}$ , where the first error comes from the lattice calculation and fit and the second is due to missing contributions from QED and isospin breaking ( $m_u \neq m_d$ ), each of which we estimate to enter at the level of 1% of the  $u/d$  piece of  $a_\mu^{\text{HVP,LO}}$ . These estimates are supported by more

TABLE III: Error budget for the connected contributions to the muon anomaly  $a_\mu$  from vacuum polarization of  $u/d$  quarks.

	$a_\mu^{\text{HVP,LO}}(u/d)$
QED corrections:	1.0%
Isospin breaking corrections:	1.0%
Staggered pions, finite volume:	0.7%
Correlator fits ( $t^*$ ):	0.5%
$m_\ell$ extrapolation:	0.4%
Monte Carlo statistics:	0.4%
Padé approximants:	0.4%
$a^2 \rightarrow 0$ extrapolation:	0.2%
$Z_V$ uncertainty:	0.2%
Correlator fits:	0.2%
Tuning sea-quark masses:	0.2%
Lattice spacing uncertainty:	< 0.05%
Total:	1.8%

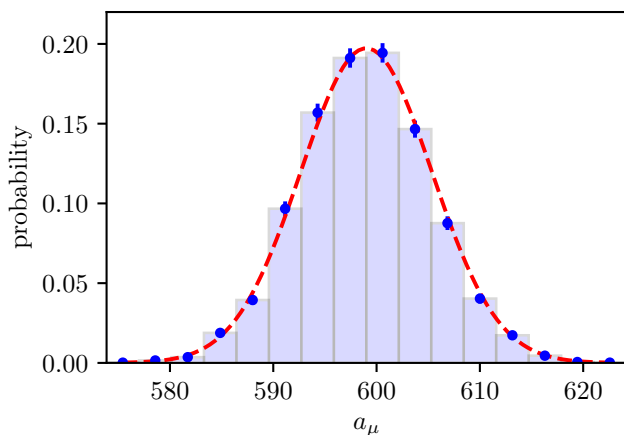


FIG. 4: Bayesian probability distribution for  $a_\mu^{\text{HVP,LO}}(u/d)$  (bars) compared with results from the least-squares fit (dashed line).

detailed studies: The key isospin breaking effect of  $\rho - \omega$  mixing is estimated in [37] to make a  $3.5 \times 10^{-10}$  contribution (0.6%) and the QED effect of producing a hadron polarization bubble consisting of  $\pi^0$  and  $\gamma$  is estimated in [38] to make a  $4.6 \times 10^{-10}$  contribution (0.8%). The leading contributions to our final uncertainty are listed in Table III. Note that our final result is 3.5% above the extrapolated result from the raw data shown in Fig. 3; most of that shift comes from corrections to the  $\pi\pi$  vacuum polarization in chiral perturbation theory.

We tested the validity of the least-squares fit that determines our  $a_\mu^{\text{HVP,LO}}(u/d)$  by replacing the fit with a Bayesian expectation value (a 16-dimensional numerical integration) over the distributions of the input data and priors. The results, in Fig. 4, show that the least-squares fit (dashed-line) agrees well with the probability distribution from the corresponding Bayesian analysis (bars).

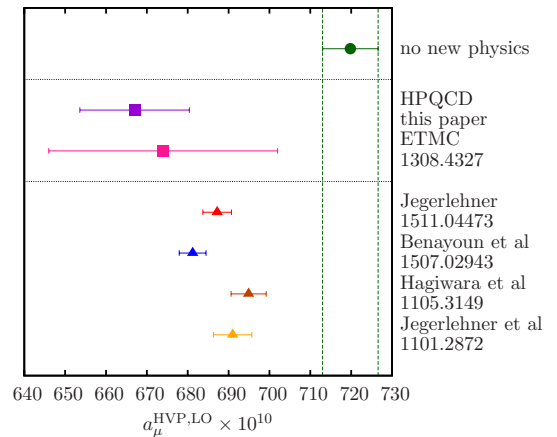


FIG. 5: Our final result for  $a_\mu^{\text{HVP,LO}}$  from lattice QCD compared to an earlier lattice result (also with  $u$ ,  $d$ ,  $s$  and  $c$  quarks) from the ETM Collaboration [13], and to recent results using experimental cross-section information [5–8]. We also compare with the result expected from the experimental value for  $a_\mu$  assuming that there are no contributions from physics beyond the Standard Model.

### III. DISCUSSION/CONCLUSIONS

Adding results from our earlier calculations for other quark flavours [14, 27], the connected contributions to  $a_\mu^{\text{HVP,LO}}$  are:

$$a_\mu^{\text{HVP,LO}}|_{\text{conn.}} \times 10^{10} = \begin{cases} 599(11) & \text{from } u/d \text{ quarks} \\ 53.4(6) & \text{from } s \text{ quarks} \\ 14.4(4) & \text{from } c \text{ quarks} \\ 0.27(4) & \text{from } b \text{ quarks} \end{cases} \quad (9)$$

We combine these results with our recent estimate [28] of the contribution from disconnected diagrams involving  $u$ ,  $d$  and  $s$  quarks, taking this as  $0(9) \times 10^{-10}$ . This agrees with, but has a more conservative uncertainty than, the value obtained in [29]. We then obtain an estimate for the entire contribution from hadronic vacuum polarization:

$$a_\mu^{\text{HVP,LO}} = 667(6)(12) \times 10^{-10} \quad (10)$$

This agrees well with the only earlier  $u/d/s/c$  lattice QCD result,  $674(28) \times 10^{-10}$  [13], but has errors from the lattice calculation reduced by a factor of four. It also agrees with earlier non-lattice results using experimental data, ranging from ( $\times 10^{10}$ ):  $694.9(4.3)$  [5] to  $681.9(3.2)$  [7]. These are separately more accurate than our result but have a spread comparable to our uncertainty. New results from BESIII [39] may resolve this.

It is also useful to compare our result to the expectation from experiment. Assuming there is no new physics beyond the Standard Model, experiment requires  $a_\mu^{\text{HVP,LO}}$  to be  $720(7) \times 10^{-10}$ . This value is obtained by subtracting from experiment the accepted values of QED [40],

electroweak [41], higher order HVP [5, 42] and hadronic light-by-light contributions [43]:

$$a_\mu^{\text{HVP,LO,no new physics}} = a_\mu^{\text{expt}} - a_\mu^{\text{QED}} - a_\mu^{\text{EW}} - a_\mu^{\text{HVP,HO}} - a_\mu^{\text{Hlbl}}. \quad (11)$$

Figure 5 compares our results with others from previous continuum and lattice analyses. We also compare with results expected from experiment if there is no new physics contributing to  $a_\mu$ . The ‘no-new-physics’ value is roughly  $3.5\sigma$  away from our result (Eq. (10)), but we need significantly smaller theoretical errors before we can make a case for new physics.

From Table III we see that uncertainties can be reduced by improving the calculation of the quark-line disconnected contribution [29, 44] and from new simulations with  $m_u \neq m_d$ ; this is straightforward. Adding QED effects to a simulation is more difficult (see, for example, [45]), but it is particularly simple here because the hadronic system is electrically neutral, so there are no infrared divergences to be dealt with<sup>1</sup>.

The remaining uncertainties are together only about 1% of our answer. The largest (0.7%) is caused by  $\alpha_s a^2$  differences in mass between pions of different taste with HISQ quarks. Reducing the lattice spacing to 0.06 fm at the physical pion mass would cut this uncertainty in half. The remaining errors would all be reduced by smaller lattice spacings and higher statistics, both of which are feasible on time scales commensurate with the schedule for the new experiments an  $a_\mu$ .

From our results we also obtain the total HVP contribution to the electron:  $a_e^{\text{HVP,LO}} = 0.01779(39) \times 10^{-10}$ , to be compared to  $0.01846(12) \times 10^{-10}$  from  $e^+e^-$  data [8].

*Acknowledgements.* We are grateful to the MILC collaboration for the use of their gauge configurations and code, to C. McNeile for updating  $w_0/a$  on set 9 and to C. DeTar, G. Donald and T. Teubner for useful discussions. Our calculations were done on the Darwin Supercomputer as part of STFC’s DiRAC facility jointly funded by STFC, BIS and the Universities of Cambridge and Glasgow. This work was funded by the Gilmour bequest to the University of Glasgow, the National Science Foundation, the Royal Society, STFC and the Wolfson Foundation. Fermilab is operated by Fermi Research Alliance, LLC under contract number DE-AC02-07CH11359 with the U.S. Department of Energy.

## Appendix A: Correlator Fits

We construct a  $2 \times 2$  matrix of meson propagators using all combinations of two meson operators, with zero three

momentum, for the source and sink. One meson operator (“loc”) is the local vector current. The other (“sm”) is a vector current but with smearing applied to the quark field, using operator

$$\left[ 1 + \frac{r_0^2 D^2}{4n} \right]^n \quad (A1)$$

where  $D^2$  is the covariant Laplacian operator and  $r_0$  is a width parameter. Since we are using staggered quarks and require current-current correlators of a specific staggered taste, we use the stride-2  $D^2$  operator here, with the difference operator defined for grid spacing  $2a$  (rather than  $a$ ). We choose  $r_0 = 3a, 3.75a$ , and  $4.5a$  for lattices spacings 0.15 fm, 0.12 fm and 0.09 fm, respectively, with  $n = 20, 30$ , and 40.

The result is a matrix of correlators,  $G_{ij}$ , where  $i$  labels the source and  $j$  the sink. Each of  $i, j$  is either “loc” for the local vector operator or “sm” for the smeared vector operator. We fit  $G_{ij}$  to the form:

$$G_{ij}(t) = a^3 \sum_{k=0}^{N-1} b_i^{(k)} b_j^{(k)} \left( e^{-E^{(k)}t} + e^{-E^{(k)}(T-t)} \right) - (-1)^t a^3 \sum_{k=0}^{N-1} d_i^{(k)} d_j^{(k)} \left( e^{-\bar{E}^{(k)}t} + e^{-\bar{E}^{(k)}(T-t)} \right) \quad (A2)$$

where  $k$  labels the energy eigenvalues appearing in the correlator and  $T$  is the temporal extent of the lattice. The first sum is over  $1^{--}$  vector states that couple to the vector operators. The second is over opposite-parity states that arise here because of our use of staggered quarks; this term oscillates in sign as  $t$  increases, which helps the fit distinguish between it and the first term. We use a Bayesian approach to the fitting [47] with the following fit parameters and broad priors (in units of GeV):

$$\begin{aligned} \log(E^{(0)}) &= \log(0.75(38)) \\ \log(E^{(k)} - E^{(k-1)}) &= \log(1.0(5)) \quad (k > 0) \\ \log(b_{\text{loc}}^{(0)}) &= \begin{cases} \log(0.14(14)) & (k = 0) \\ \log(0.42(42)) & (k > 0) \end{cases} \\ b_{\text{sm}}^{(0)}, b_{\text{sm}}^{(k)} &= 0.01(1) \end{aligned} \quad (A3)$$

for the first sum, and the analogous parameters and priors for the second sum but with

$$\log(\tilde{E}^{(0)}) = \log(1.2(6)), \quad (A4)$$

to reflect the higher mass of the lowest opposite-parity state. To avoid lattice artifacts (from the HISQ action) at very small times, we fit the correlators only for  $t$  values larger than 0.5–0.7 fm. We used  $N = 5$ , but get identical results with larger values of  $N$ . The fits were all excellent, with  $\chi^2$  per degree of freedom ranging between 0.6 and 1.1 in different fits. The use of a smeared operator improves the fit results for  $E^{(0)}$  and  $b_{\text{loc}}^{(0)}$  (from which we

<sup>1</sup> There are higher order QED effects where the photon interacts with both  $\mu$  and hadrons (the ‘hadronic light-by-light’ contribution) which are more complicated—lattice QCD also shows promise here [46].

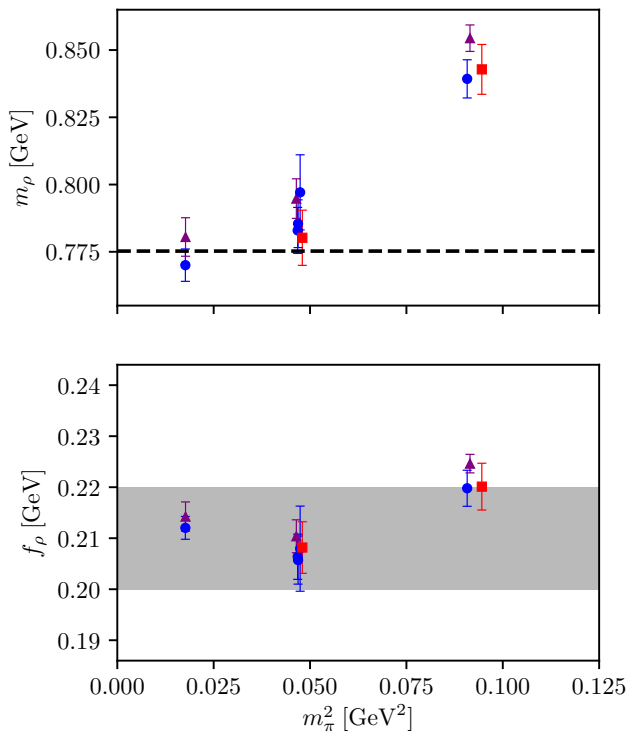


FIG. 6: Results for the  $\rho$  meson mass (upper plot) and decay constant (lower plot) from the vector correlators used to determine the  $u/d$  connected contribution to  $a_\mu^{\text{HVP,LO}}$ . Results are shown for different  $u/d$  masses, as indicated by the corresponding values of  $m_\pi^2$  (the lightest being the physical value). Data come from simulations with lattice spacings of 0.15 fm (purple triangles), 0.12 fm (blue circles), and 0.09 fm (red squares). Experimental results for the mass (dashed line) and decay constant (gray band) are shown as well. A comparison of our results with those of [11, 13] is given in [48].

obtain our values for  $m_\rho$  and  $f_\rho$ ) by an amount commensurate with its numerical cost.

As discussed in the main text, we use a combination of data and fit results when computing moments of the local current-current correlator  $G \equiv G_{\text{loc,loc}}$ :

$$G(t) = \begin{cases} G_{\text{data}}(t) & t \leq t^* \\ G_{\text{fit}}(t) & t > t^* \end{cases} \quad (\text{A5})$$

where we define

$$G_{\text{fit}}(t) = a^3 \sum_{k=0}^{N-1} b_{\text{loc}}^{(k)} b_{\text{loc}}^{(k)} e^{-E^{(k)}t} - (-1)^t a^3 \sum_{k=0}^{N-1} d_{\text{loc}}^{(k)} d_{\text{loc}}^{(k)} e^{-\tilde{E}^{(k)}t} \quad (\text{A6})$$

with the best-fit values for the parameters.  $G_{\text{fit}}$  is the same as  $G_{\text{loc,loc}}$  from Eq. (A2) but with  $T \rightarrow \infty$ , thereby correcting for the finite temporal extent of the lattice. Note that about 80% of our final result for  $a_\mu$  comes

from  $t \leq t^*$  ( $=1.5$  fm), where we use simulation data rather than our fit.

The sum over states in  $G_{\text{fit}}$  (above) includes vector mesons like the  $\rho$  and also multi-hadron states, which enter as discrete energy eigenstates because of the finite spatial volume of our lattice. The lowest-energy states are  $\pi\pi$  states for configurations with physical pion masses, but we see no evidence of these in our fits—the dominant contribution comes from the  $\rho$  meson. This is expected because there are only a few  $\pi\pi$  states below the  $\rho$  mass, and their contribution is suppressed by a factor of one over the lattice volume (see Eq. (B32) below), making their contributions to  $a_\mu$  smaller than our statistical errors. Note that it has been possible to see coupled  $\rho$  and  $\pi\pi$  states in lattice QCD calculations (see, for example, [49]) but to do so requires careful meson and multi-meson operator optimization to achieve measurable overlaps; the calculations do not use the local vector current that is relevant here.

The contribution of the low-energy  $\pi\pi$  states coming from  $t \leq t^*$  is included in our calculation, since we use the Monte Carlo results in that region. The contribution from  $t > t^*$ , however, is underestimated or missing. That contribution can be calculated using the chiral formalism developed below. We find that the low-energy  $\pi\pi$  contribution from  $t > t^*$  should be  $3 \times 10^{-10}$  when  $t^* = 1.5$  fm (our default value), and so we include an uncertainty of  $\pm 3 \times 10^{-10}$  in our error budget for  $a_\mu$  to account for these states. This estimate is for configuration set 8 in Table I, where the uncertainty is largest, so it is probably an overestimate of the impact on the entire calculation.

The  $t > t^*$  contribution from low-energy  $\pi\pi$  states would be twice as large had we chosen  $t^* = 0.5$  fm, and therefore the difference

$$\delta a_\mu \equiv a_\mu(t^* = 0.5) - a_\mu(t^* = 1.5) \quad (\text{A7})$$

provides an upper bound on the possible error caused by omitting these states from  $G_{\text{fit}}$ . Redoing our full analysis for  $t^* = 0.5$  fm, we find that  $\delta a_\mu = 0 \pm 3 \times 10^{-10}$ , which is consistent with our direct estimate from chiral perturbation theory.

An important check on the quality of our correlators and fit is that the  $\rho$  mass and decay constant agree with experiment when the light quarks have their physical values. This is illustrated by Figure 6, which shows the mass and decay constants from each of our configuration sets. Theory and experiment agree to within errors for physical quark masses.<sup>2</sup>

<sup>2</sup> The definition of  $f_\rho$  is complicated by the large width of the  $\rho$  meson. Applying naive definitions gives results around 0.208 GeV from  $\tau$  decay and around 0.220 GeV from  $\rho \rightarrow e\bar{e}$ , with errors of order a couple percent in each case. A more careful analysis, which models non-resonant backgrounds in each case, is needed to resolve the differences between these two channels. We take the experimental value to be  $f_\rho = 0.21(1)$  GeV for Figure 6.



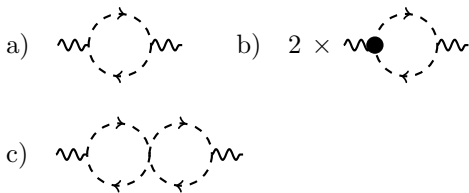


FIG. 7: Leading diagrams from chiral perturbation theory that contribute to  $\delta\Pi_j$ : a) leading-order  $\pi^+\pi^-$  vacuum polarization; b) vacuum polarization corrected for the pion's charge radius; c)  $\pi\pi$  scattering correction. Dashed lines represent pions.

## Appendix B: Finite Volume and Staggered Pions

We use chiral perturbation theory to correct systematic errors in our lattice results caused by the finite volumes of our lattices, and by mass splittings between the different tastes of pion generated by our (staggered-quark) HISQ discretization. Our general strategy is to identify terms in the chiral expansion that are sensitive to the volume and to pion masses (i.e., loops with pions). We calculate these terms without and with lattice artifacts, and then add the difference to the lattice results.

The only relevant contribution from zeroth order in the chiral expansion is the  $\pi^+\pi^-$  vacuum polarization (Fig. 7a). As expected, we find that it provides most of the correction.

There are three types of higher-order correction beyond this term. The first two involve corrections (from, for example, tadpole diagrams) to the leading vacuum polarization diagram that are suppressed by powers of either the strange or the light-quark masses. Such corrections are typically of order 10% the leading contribution for  $s$  quarks and 1% for  $u/d$  quarks. We include an extra 10% uncertainty in our corrections to account for such contributions.

The third type of correction involves terms suppressed by powers of  $q^2/\Lambda^2$  where  $\Lambda$  is the chiral scale ( $\approx 1$  GeV). Such terms are easily analyzed in our formalism, because it relies on moments. They enter in first order as corrections to the  $\gamma\pi\pi$  vertex due to the pion's charge radius (Fig. 7b).  $\pi\pi$  scattering (Fig. 7c) also enters at this order, but is much less important, as we shall see. Second-order and higher contributions come from further corrections to the vertices, iterations of the leading diagrams, and so on. These give small contributions compared with our errors.

Our analysis is simplified by using an extended version of standard chiral perturbation theory that includes  $\gamma s$ ,  $\pi s$ , and  $\rho s$  [50, 51]. Such a theory is particularly useful here because  $\gamma$ - $\rho$  mixing accounts for the bulk of the vacuum polarization contribution to the muon anomaly. In the next section we examine  $\gamma$ - $\rho^0$ - $\pi^+\pi^-$  mixing to all orders in the leading interactions that couple these channels. This analysis includes all of the contributions illustrated in Fig. 7, as well as all iterations of these di-

agrams. It also includes an infinite number of  $(q^2/m_\rho^2)^n$  corrections.

Following [6], we make one further simplification in our analysis that allows us, in effect, to absorb the 4-pion contact interaction into the amplitude for  $\pi\pi \rightarrow \rho \rightarrow \pi\pi$ . This is done by replacing the chiral  $\rho$ - $\pi\pi$  coupling by a simpler coupling,  $-ig_{\rho\pi\pi}(p+p')^\mu$ , analogous to the photon coupling. The resulting  $\pi\pi$  scattering amplitude, which now comes entirely from  $\pi\pi \rightarrow \rho \rightarrow \pi\pi$ , is equivalent to what is obtained from the chiral theory, but simpler to analyze, at least for our application.

It is well known that chiral parameters for the  $\rho$  channel in  $\pi\pi$  scattering are more or less saturated by the  $\rho$  itself [51]. Our analysis relies upon this fact as it uses high-order chiral coefficients determined by the  $\rho$ . After the pion charge and mass, the most important parameter for our results is the pion charge radius. The model we use below gives a pion charge radius squared of  $0.46 \text{ fm}^2$ , which agrees well with experiment at  $0.45(1) \text{ fm}^2$  [52]. Similarly the  $P$ -wave scattering length for  $\pi\pi$  scattering in our model is  $0.037/m_\pi^3$ , which again compares well with experiment at  $0.038(2)/m_\pi^3$  (see, for example, [53] and [54].) These comparisons show that the parameters in the effective theory are tuned sufficiently well for our purposes.

In the next section we derive a photon propagator that takes account of  $\gamma$ - $\rho^0$ - $\pi^+\pi^-$  mixing in our effective field theory. We then specialize that result for use in analyzing  $a_\mu$ . Finally we show how these results are affected by the lattice's finite volume and by taste-splittings between HISQ pions. This allows us to correct the moments from our simulation to remove systematic errors from finite volumes and staggered pions.

### 1. Photon propagator

The one-loop corrected  $\rho$  and photon propagators of the effective theory,

$$G(q) \equiv \begin{pmatrix} G_{\gamma\gamma}(q) & G_{\gamma\rho}(q) \\ G_{\rho\gamma}(q) & G_{\rho\rho}(q) \end{pmatrix}, \quad (\text{B1})$$

are obtained by solving a matrix Lippmann-Schwinger equation,

$$G = G_0 - G_0 \Sigma G, \quad (\text{B2})$$

where

$$\Sigma = q^2 \begin{pmatrix} \Sigma_{\gamma\gamma}^{(1)} & e/g_\rho + \Sigma_{\gamma\rho}^{(1)} \\ e/g_\rho + \Sigma_{\rho\gamma}^{(1)} & \Sigma_{\rho\rho}^{(1)} \end{pmatrix}. \quad (\text{B3})$$

Here we project onto a transverse polarization to remove the spin algebra. The lowest-order propagator is

$$G_0 = \begin{pmatrix} q^2 & 0 \\ 0 & q^2 - m_{0\rho}^2 \end{pmatrix}^{-1}, \quad (\text{B4})$$

while the leading-order  $\pi\pi$  loops give amplitudes [6]

$$\begin{aligned}\Sigma_{\gamma\gamma}^{(1)} &= e^2 \Sigma(q^2) \\ \Sigma_{\rho\rho}^{(1)} &= eg_{\rho\pi\pi} \Sigma(q^2) \quad \Sigma_{\rho\rho}^{(1)} = g_{\rho\pi\pi}^2 \Sigma(q^2)\end{aligned}\quad (\text{B5})$$

where

$$\begin{aligned}48\pi^2 \Sigma(q^2) \\ = \frac{2}{3} + 2(1-y) - 2(1-y)^2 G(y) + \log(\mu^2/m_\pi^2),\end{aligned}\quad (\text{B6})$$

$y \equiv 4m_\pi^2/q^2$ , and

$$G(y) = \begin{cases} \frac{1}{2\sqrt{1-y}} \left( \log \frac{1+\sqrt{1-y}}{1-\sqrt{1-y}} - i\pi \right) & \text{for } y < 1, \\ -\frac{1}{\sqrt{y-1}} \arctan(1/\sqrt{y-1}) & \text{for } y > 1. \end{cases}\quad (\text{B7})$$

We normalize results from [6] at  $\mu = m_\pi$ .

We are particularly interested in the corrected photon propagator from this theory, since that is what enters  $g-2$ . Solving the Lippmann-Schwinger equation gives:

$$\begin{aligned}G_{\gamma\gamma} &= \frac{1}{q^2 (1 + \Sigma_{\gamma\gamma}^{(1)})} + \\ &\frac{(e/g + \Sigma_{\gamma\rho}^{(1)})^2}{q^2 \left( 1 + \Sigma_{\rho\rho}^{(1)} - (e/g + \Sigma_{\gamma\rho}^{(1)})^2 \right) - m_{0\rho}^2},\end{aligned}\quad (\text{B8})$$

where we have dropped a factor of  $1 + \Sigma_{\gamma\gamma}^{(1)}$  in the denominator of the last term since it enters only in order  $e^4$ .

This propagator has poles at  $q^2 = 0$  and at the (renormalized)  $\rho$  mass. We can set the coupling constants from the behavior near the  $\rho$  pole, where

$$G_{\gamma\gamma}(q) \rightarrow \frac{e^2 f_\rho^2}{2m_\rho^2} \frac{1}{q^2 - m_\rho^2 + im_\rho \Gamma_\rho}.\quad (\text{B9})$$

Here  $f_\rho$  is the  $\rho$ 's decay constant, and  $\Gamma_\rho$  is its width. Comparing these two expressions we find that:

$$m_\rho^2 - im_\rho \Gamma_\rho = m_{0\rho}^2 (1 - g_{\rho\pi\pi}^2 \Sigma(m_\rho^2))\quad (\text{B10})$$

and

$$\begin{aligned}\frac{f_\rho}{\sqrt{2} m_\rho} &= \frac{1/g_\rho + g_{\rho\pi\pi} \Sigma(m_\rho^2)}{1 + \frac{1}{2} g_{\rho\pi\pi}^2 \Sigma(m_\rho^2) + \frac{1}{2} g_{\rho\pi\pi}^2 m_\rho^2 \Sigma'(m_\rho^2)} \\ &\approx \frac{1}{g_\rho} \left( 1 + g_\rho g_{\rho\pi\pi} \Sigma(m_\rho^2) - \frac{1}{2} g_{\rho\pi\pi}^2 \Sigma(m_\rho^2) \right. \\ &\quad \left. - \frac{1}{2} g_{\rho\pi\pi}^2 m_\rho^2 \Sigma'(m_\rho^2) \right)\end{aligned}\quad (\text{B12})$$

up to QED corrections suppressed by  $\alpha_{\text{QED}}$ . Here

$$48\pi^2 q^2 \Sigma'(q^2) = 3y - 1 - 3y(1-y)G(y)\quad (\text{B13})$$

where, again,  $y \equiv 4m_\pi^2/q^2$ . Taking

$$\begin{aligned}m_\rho &= 0.775 \text{ GeV} \quad \Gamma_\rho = 0.148 \text{ GeV} \quad f_\rho \approx 0.21 \text{ GeV} \\ m_\pi &= m_{\pi^+} = 0.1396 \text{ GeV},\end{aligned}\quad (\text{B14})$$

we find the bare parameters are:

$$m_{0\rho} = 0.766 \text{ GeV} \quad g_\rho = 5.4 \quad g_{\rho\pi\pi} = 6.0.\quad (\text{B15})$$

## 2. Contribution to $g-2$

Returning to the photon propagator, we find that

$$G_{\gamma\gamma} \rightarrow \frac{Z_{\text{had}}}{q^2 (1 - e^2 \hat{\Pi}(q))}\quad (\text{B16})$$

near the photon pole, where

$$Z_{\text{had}} = \frac{1}{1 - e^2 \Pi(0)},\quad (\text{B17})$$

$\hat{\Pi}(q) \equiv \Pi(q) - \Pi(0)$ , and

$$\Pi(q^2) = -\Sigma(q^2) + \frac{q^2 (1/g_\rho + g_{\rho\pi\pi} \Sigma(q^2))^2}{q^2 (1 + g_{\rho\pi\pi}^2 \Sigma(q^2)) - m_{0\rho}^2}\quad (\text{B18})$$

This can be rewritten

$$\begin{aligned}\hat{\Pi}(q^2) &= -\hat{\Sigma}(q^2) \\ &+ \frac{\hat{f}^2}{2\hat{m}^2} \frac{q^2 (1 + g_\rho g_{\rho\pi\pi} \hat{\Sigma}(q^2))^2}{q^2 (1 + g_{\rho\pi\pi}^2 \hat{\Sigma}(q^2)) - \hat{m}^2}\end{aligned}\quad (\text{B19})$$

where  $\hat{\Sigma}(q^2) \equiv \text{Re} \Sigma(q^2) - \Sigma(0)$ ,

$$\hat{m}^2 \equiv m_0^2 (1 - g_{\rho\pi\pi}^2 \Sigma(0))\quad (\text{B20})$$

$$= m_\rho^2 \left( 1 + g_{\rho\pi\pi}^2 \hat{\Sigma}(m_\rho^2) \right),\quad (\text{B21})$$

and

$$\begin{aligned}\frac{\hat{f}}{\hat{m}} &\equiv \frac{\sqrt{2}}{g_\rho} \left( 1 + g_\rho g_{\rho\pi\pi} \Sigma(0) - \frac{1}{2} g_{\rho\pi\pi}^2 \Sigma(0) \right) \\ &\approx \frac{f_\rho}{m_\rho} \left( 1 - \frac{1}{2} g_{\rho\pi\pi}^2 \hat{\Sigma}(m_\rho^2) + \frac{1}{2} g_{\rho\pi\pi}^2 m_\rho^2 \hat{\Sigma}'(m_\rho^2) \right)\end{aligned}\quad (\text{B22})$$

are all independent of the ultraviolet regulator. We approximated  $g_\rho \rightarrow g_{\rho\pi\pi}$  in the last line above, to simplify the result. Values for  $\hat{f}$  and  $\hat{m}$  equal those for  $f_\rho$  and  $m_\rho$  to within a few percent.

To compute the contribution to  $g-2$  from  $\hat{\Pi}(q)$ , we Taylor expand and switch to Euclidean momenta ( $q^2 \rightarrow -q_E^2$ ):

$$\hat{\Pi}(-q_E^2) \equiv \sum_{j=1}^{\infty} q_E^{2j} \Pi_j,\quad (\text{B24})$$

where  $\Pi_j = \Pi_j^{(\pi\pi)} + \Pi_j^{(\rho)}$ , corresponding to the first and second terms in Eq. (B19), respectively.

To leading order,

$$\Pi_j^{(\pi\pi)} = \frac{(-1)^{j+1} (j+1)! (j-1)!}{8\pi^2 m_\pi^{2j} (2j+3)!},\quad (\text{B25})$$

$$\Pi_j^{(\rho)} = \frac{(-1)^{j+1} f_\rho^2}{2m_\rho^{2j+2}} + \mathcal{O}(g_{\rho\pi\pi}^2)\quad (\text{B26})$$

Substituting these results into our formalism for  $g = 2$ , with  $m_\pi = m_{\pi^+} = 0.13957$ , gives the leading contributions from  $\pi\pi$  loops and from the  $\rho$ :

$$a_\mu^{(\pi\pi)} = 71 \times 10^{-10} \quad (\text{B27})$$

$$a_\mu^{(\rho)} = 425 \times 10^{-10} + \mathcal{O}(g_{\rho\pi\pi}^2) \quad (\text{B28})$$

This shows that the  $\rho$  by itself accounts for about 71% of the total vacuum polarization contribution to  $a_\mu$ , with  $\pi\pi$  interactions adding another 12%.

### 3. Lattice Corrections

Lattice simulations modify the low-energy analysis given above in two ways: 1) the lattice volume is finite; and 2) pion-loop results are averaged over several tastes of pion, each with a different mass. The second of these is peculiar to formalisms, like HISQ, that use staggered quarks. These effects are largest in the  $\pi\pi$  vacuum polarization function. To correct for these simulation artifacts, we reexamine the  $\pi\pi$  contribution to  $\frac{1}{3} \sum_i \Pi_{ii}^{(\pi\pi)}(q_E^2)$  in continuum Euclidean QCD:

$$\frac{4}{3} \int \frac{d^4k}{(2\pi)^4} \frac{k^2 - k_0^2}{(k^2 + m_a^2)(k^2 + 2k_0q_E + q_E^2 + m_b^2)} \quad (\text{B29})$$

$$= \frac{4}{3} \int \frac{d^3\mathbf{k}}{(2\pi)^3} \frac{(E_a + E_b) \mathbf{k}^2}{2E_a E_b q_E^2 + (E_a + E_b)^2} \quad (\text{B30})$$

where  $q_\mu = q^\mu = (q_E, 0, 0, 0)$ ,  $E_i = \sqrt{\mathbf{k}^2 + m_i^2}$ , and normally  $m_a = m_b = m_\pi$ . This implies that the  $\pi\pi$  vacuum polarization function used in the previous section is given by:

$$-\hat{\Sigma}(-q_E^2, m_a, m_a) \equiv \frac{4q_E^2}{3} \int \frac{d^3\mathbf{k}}{(2\pi)^3} \frac{\mathbf{k}^2}{2E_a E_b (E_a + E_b)^3 (q_E^2 + (E_a + E_b)^2)}. \quad (\text{B31})$$

The Taylor coefficients  $\Pi_j^{(\pi\pi)}$  derived in the previous section are the coefficients of  $q_E^{2j}$  in the expansion of this expression when  $m_a = m_b = m_\pi$ .

We correct for the finite spatial volume ( $L^3$ ) of the lattice by replacing

$$\int \frac{d^3\mathbf{k}}{(2\pi)^3} \rightarrow \frac{1}{L^3} \sum_{k_x=-\infty}^{\infty} \sum_{k_y=-\infty}^{\infty} \sum_{k_z=-\infty}^{\infty} \quad (\text{B32})$$

where the sums are over discrete momenta  $k = 2\pi n/L$  for all integer  $n$ , positive and non-positive. (We correct our fits separately for the finite temporal length of the lattice, which is, in any case, 1.5–3 times longer than in spatial directions and so effectively infinite.) We ignore the effect of the finite lattice spacing since the contributions of interest are all ultraviolet finite (and quite infrared).

The second modification concerns the pion masses in the vacuum polarization, and is specific to staggered-quark actions like the HISQ action we use. In our simulations we use vector currents  $J_\mu$  that are local, which means that they carry taste  $\xi_\mu$ . (We use the notation of [34], which discusses quark doubling and taste symmetry at length, especially in Appendices A–D.) Taste conservation means that the pion pairs must carry the same total taste as the current but there are several different taste pairings that accomplish this. A current with total taste  $\xi_\mu$  can couple to pion pairs carrying tastes:

1.  $\xi_5 \oplus \xi_{\mu 5}$  (2 combinations);
2.  $\xi_{\nu 5} \oplus \xi_{\rho\sigma}$  where  $\mu, \nu, \rho$ , and  $\sigma$  are all different (6 combinations);
3.  $\xi_{\rho\sigma} \oplus \xi_\nu$  where  $\rho = \mu \neq \nu = \sigma$  (6 combinations);
4.  $\xi_\mu \oplus 1$  (2 combinations).

The total contribution is the average over these 16 possibilities. We estimate the  $\pi\pi$  contribution to the vacuum polarization in our simulations by averaging over the contributions Eq. (B31) from each pairing of pion tastes, with  $m_a$  and  $m_b$  set to the masses of the two pions. We use pion masses for different tastes derived from MILC's results in [55] (see Table IV).

In Table IV we list corrections  $\delta\Pi_j$  for the moments from each of our configuration sets. We add these to the Monte Carlo results in order to correct for effects due to the finite volume and pion-mass taste splittings. We estimate these corrections by approximating Eq. (B19) with

$$\hat{\Pi}(-q_E^2, f_\rho, m_\rho, m_\pi) = -\hat{\Sigma}(-q_E^2, m_\pi, m_\pi) + \frac{f_\rho^2}{2m_\rho^2} \frac{q_E^2 \left(1 + g_\rho g_{\rho\pi\pi} \hat{\Sigma}(-q_E^2, m_\pi, m_\pi)\right)^2}{q_E^2 \left(1 + g_{\rho\pi\pi}^2 \hat{\Sigma}(-q_E^2, m_\pi, m_\pi)\right) + m_\rho^2} \quad (\text{B33})$$

where  $\hat{\Sigma}$  is the  $\pi^+\pi^-$  vacuum polarization function from Eq. (B31), and we have replaced  $\hat{f}$  and  $\hat{m}$  by  $f_\rho$  and  $m_\rho$ , respectively. To obtain the correction for a given configuration set, we first evaluate this continuum vacuum polarization function using the (Goldstone)  $m_\pi$ ,  $m_\rho$ , and  $f_\rho$  obtained from the configuration set (Table I), and then we subtract from it the same quantity but with

$$\hat{\Sigma}(-q_E^2, m_\pi, m_\pi) \rightarrow \frac{1}{16} \sum_{\xi_a, \xi_b} \hat{\Sigma}_V(-q_E^2, m_\pi(\xi_a), m_\pi(\xi_b)) \quad (\text{B34})$$

where  $\hat{\Sigma}_V$  is evaluated for the finite volume of the configuration (Eq. (B32)), and averaged over the staggered-pion taste combinations  $\xi_a \oplus \xi_b$  listed above. The corrections  $\delta\Pi_j$  are the Taylor coefficients of this difference between continuum and finite-volume/staggered-pion vacuum polarizations.

The contribution to  $a_\mu$  from the first term in Eq. (B33) is roughly five times larger than that from the second

TABLE IV: Pion masses for different tastes, and the corresponding finite-volume plus staggered-pion corrections to be added to the Taylor coefficients  $\Pi_j$  for each configuration (as given in Table II). The pion masses are based upon results in [55], using our definition of the lattice spacing. The Taylor coefficients include an extra 10% uncertainty, beyond that due to uncertainties in the pion masses, to account for uncalculated and partially calculated higher-order terms in chiral perturbation theory.

Set	$m_\pi(\xi_5)$	$m_\pi(\xi_{5\mu})$	$m_\pi(\xi_{\mu\nu})$	$m_\pi(\xi_\mu)$	$m_\pi(1)$	$\delta\Pi_1$	$\delta\Pi_2$	$\delta\Pi_3$	$\delta\Pi_4$
1	0.302(2)	0.362(3)	0.407(4)	0.451(5)	0.485(19)	0.0012(1)	-0.0050 (5)	0.014 (1)	-0.034 (4)
2	0.216(1)	0.294(3)	0.348(4)	0.399(6)	0.438(23)	0.0028(3)	-0.0160(16)	0.063 (7)	-0.220 (24)
3	0.133(1)	0.240(3)	0.304(5)	0.362(7)	0.405(26)	0.0094(9)	-0.0836(86)	0.588(62)	-4.320(472)
4	0.301(2)	0.334(2)	0.360(3)	0.390(4)	0.413 (9)	0.0008(1)	-0.0038 (4)	0.012 (1)	-0.029 (3)
5	0.218(1)	0.262(2)	0.295(3)	0.331(4)	0.359(11)	0.0025(2)	-0.0141(15)	0.056 (6)	-0.196 (22)
6	0.217(1)	0.261(2)	0.294(3)	0.331(4)	0.358(11)	0.0022(2)	-0.0131(13)	0.054 (6)	-0.196 (22)
7	0.216(1)	0.261(2)	0.294(3)	0.330(4)	0.358(11)	0.0021(2)	-0.0125(13)	0.052 (6)	-0.191 (21)
8	0.133(1)	0.197(2)	0.240(4)	0.284(5)	0.316(13)	0.0081(8)	-0.0771(79)	0.571(60)	-4.340(474)
9	0.308(2)	0.319(2)	0.328(2)	0.337(2)	0.345 (4)	0.0005(1)	-0.0026 (3)	0.008 (1)	-0.021 (2)
10	0.219(1)	0.235(1)	0.247(2)	0.259(3)	0.270 (5)	0.0013(1)	-0.0084 (9)	0.038 (4)	-0.148 (16)

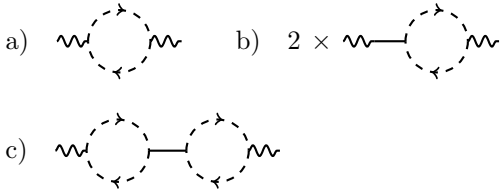


FIG. 8: Leading diagrams from the  $\rho$  effective field theory that correspond (to leading order in  $q^2/m_\rho^2$ ) to the diagrams in Fig. 7 from the standard chiral theory: a) leading-order  $\pi^+\pi^-$  vacuum polarization; b) correction for the pion's charge radius from  $\gamma \rightarrow \rho \rightarrow \pi\pi$ ; c) correction for  $\pi\pi$  scattering from  $\pi\pi \rightarrow \rho \rightarrow \pi\pi$ . Dashed and solid lines represent pions and rhos, respectively.

term, and has the opposite sign. This is for our simulation results with physical pion masses and the intermediate lattice spacing (set 8). The largest contributions come mainly from the terms

$$-\hat{\Sigma}(-q_E^2, m_\pi, m_\pi) \times \left(1 - g_\rho g_{\rho\pi\pi} \frac{f_\rho^2}{m_\rho^2} \frac{q_E^2}{m_\rho^2}\right) \quad (\text{B35})$$

$$= -\hat{\Sigma}(-q_E^2, m_\pi, m_\pi) \times \left(1 - \frac{\langle r_\pi^2 \rangle q_E^2}{3}\right) \quad (\text{B36})$$

in Eq. (B33) (Figs. 8a and 8b), where  $r_\pi$  is the charge radius of the pion. They contribute corrections to  $a_\mu$  of  $50 \times 10^{-10}$  and  $-13 \times 10^{-10}$ , respectively. Further  $(q^2/m_\rho^2)^n$  corrections to the  $\gamma$ - $\pi\pi$  vertex contribute  $3 \times 10^{-10}$ . The other  $q_E^2/m_\rho^2$  correction in Eq. (B33) is from  $\pi\pi$  scattering (Fig. 8c):

$$\frac{f_\rho^2}{2m_\rho^2} \frac{q_E^2}{m_\rho^2} \left(g_\rho g_{\rho\pi\pi} \hat{\Sigma}(-q_E^2, m_\pi, \pi)\right)^2. \quad (\text{B37})$$

This should be small because it is second order in  $g_\rho g_{\rho\pi\pi} \hat{\Sigma}$ ; in fact, it contributes less than  $0.5 \times 10^{-10}$ . The total correction from all contributions (to all orders) is  $41 \times 10^{-10}$  for set 8—chiral perturbation theory converges relatively rapidly here.

We add an extra 10% uncertainty to each correction  $\delta\Pi_j$  to account for missing contributions suppressed by  $m_s/\Lambda$ , due to tadpole and other renormalizations of the leading vacuum polarization. This uncertainty also accounts for corrections of order  $(q^2/\Lambda)^2$  and higher that are only partially included by our analysis.

The taste structure of the  $\pi\pi$  vacuum polarization matters because its contribution to  $a_\mu$  is quite sensitive to the pion mass (see Eq. (B25)) and pions of different taste differ in mass. Taste-changing interactions normally lead to small corrections that extrapolate smoothly to zero, like  $\alpha_s(\pi/a) a^2$ , as the lattice spacing vanishes. This does not work for the  $\pi\pi$  vacuum polarization with physical pions, however, because its moments are non-analytic in  $m_\pi$  (Eq. (B25)) and the taste-changing effects are comparable to the (physical) pion mass. This is why we use chiral perturbation theory to remove the effects of the staggered pion masses in the  $\pi\pi$  vacuum polarization. There are other effects from taste-changing but we only need correct contributions that are non-analytic in  $m_\pi$  (and large enough to matter); all other effects will extrapolate away as we take the lattice spacing to zero. The  $a$ -independence of our final results is evidence that we have handled these corrections properly.

As noted in the main text, the largest corrections (7%) are for our lightest pion masses. Corrections for our heaviest pions are about an order of magnitude smaller, and therefore negligible compared to other errors. The corrections are also negligible for  $s$ -quark vacuum polarization, as discussed in our previous paper [14].

We tested our finite-volume analysis by analyzing simulations with three different volumes for our intermediate lattice spacing and a pion mass of about 220 MeV (configuration sets 5–7). The raw data show variations between the three volumes of 3.1(1.3)%. Our corrections, from finite-volume/staggered-pion-masses and  $\rho$ -mass rescaling, reduce this variation by an order of magnitude; see Figure 3. This is a non-trivial test of our corrections.

We also tested our finite-volume/staggered-pion corrections by comparing results for individual Taylor coefficients with experiment. Fig 9 shows the corrected

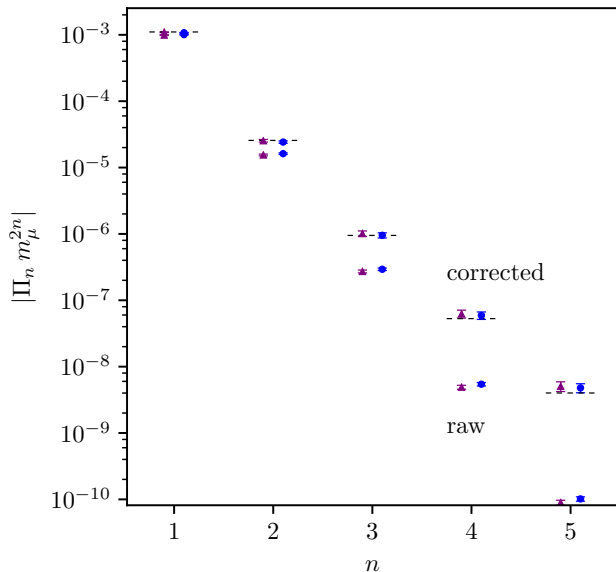


FIG. 9: Contributions to the hadronic vacuum polarization  $\hat{\Pi}(q^2)$  at  $q^2 = -m_\mu^2$  coming from individual Taylor coefficients  $\Pi_n$  with  $n = 1 \dots 5$ . Results are shown for corrected (above) and uncorrected (“raw”, below) coefficients coming from our lattice QCD simulations with physical sea-quark masses (sets 3 and 8). The corrected coefficients include both corrections described in Section II B: 1) adding  $\delta\Pi_n$  from Table IV; and 2) replacing the pion mass from the simulation with the physical pion mass in the leading  $\pi\pi$  loop. To compare with experiment, we add contributions from  $s$  and  $c$  quarks [14] to both the raw and corrected moments, neglecting their contribution to the  $n = 5$  moment (which is negligible). The dashed lines are results derived from  $e^+e^-$  data: see the “data direct” column in Table I of [56]. The error estimates on the lattice results do not include contributions due to electromagnetic, isospin-violating, and disconnected contributions; (estimated to be around 2% for the  $n = 1$  moment).

lattice results, combined with  $s$  and  $c$  quark contributions from [14], together with results based on data from  $e^+e^-$  annihilation [56]. The agreement is strong evidence that our estimates for these corrections are reliable. Note that the corrections for moments with  $n \geq 3$  are larger

than the uncorrected results from the simulation. These large- $n$  moments have negligible impact on  $a_\mu$  ( $\leq 0.5\%$ ), but they provide sensitive tests of our corrections.

The  $\delta\Pi_j$  are almost entirely due to the staggering of the pion masses. Normally one would expect larger finite-volume errors, but here the average pion mass appearing in any  $\pi\pi$  vacuum polarization contribution is larger than the physical pion mass because of the staggering. This strongly suppresses finite-volume effects. Fig. 10 shows how the uncertainty from this correction depends upon the taste-splittings between pions  $\Delta m_\pi^2$  and the spatial size  $L$  of the lattice. Lines are drawn for varying  $\Delta m_\pi^2$  at physical pion mass starting from coarse set 8. The uncertainty shown in the figure for the largest  $\Delta m_\pi^2$  is

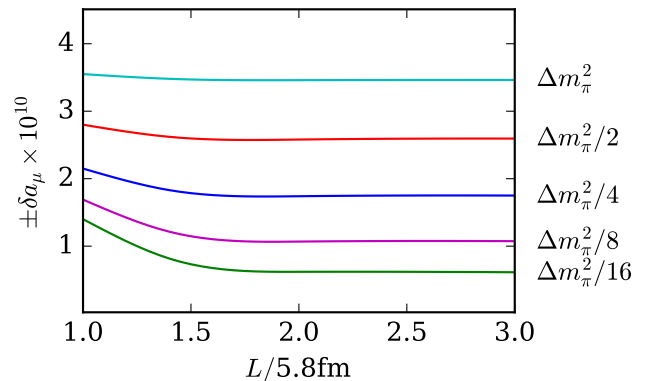


FIG. 10: Uncertainty in  $a_\mu^{\text{HVP,LO}}$  due to finite-volume and staggered-pion effects as a function of the average taste-splitting  $\Delta m_\pi^2$  between pions and the spatial size  $L$  of the lattice at the physical value of  $m_{\pi^+}$  (140 MeV). Here the line marked  $\Delta m_\pi^2$  refers to the splittings for configuration set 8 in Table IV for which  $L = 5.8$  fm. The splittings decrease slightly faster than  $a^2$  as the lattice spacing decreases, so the other lines shown correspond to conservative uncertainties at lattice spacings of approximately 0.09 fm, 0.06 fm, 0.045 fm and 0.03 fm. The uncertainties are estimated to be 1/10 of the correction.

somewhat smaller than the uncertainty that we use for configuration set 8 because the pion mass on that ensemble is smaller than the physical pion mass.

[1] G. Bennett et al. (Muon G-2 Collaboration), Phys.Rev. **D73**, 072003 (2006), hep-ex/0602035.  
[2] G. Venanzoni, Frascati Phys.Ser. **54**, 52 (2012), 1203.1501.  
[3] T. Blum, A. Denig, I. Logashenko, E. de Rafael, B. Lee Roberts, et al. (2013), 1311.2198.  
[4] M. Davier, A. Hoecker, B. Malaescu, and Z. Zhang, Eur.Phys.J. **C71**, 1515 (2011), 1010.4180.  
[5] K. Hagiwara, R. Liao, A. D. Martin, D. Nomura, and T. Teubner, J.Phys. **G38**, 085003 (2011), 1105.3149.  
[6] F. Jegerlehner and R. Szafron, Eur. Phys. J. **C71**, 1632

(2011), 1101.2872.  
[7] M. Benayoun, P. David, L. DelBuono, and F. Jegerlehner, Eur. Phys. J. **C75**, 613 (2015), 1507.02943.  
[8] F. Jegerlehner, EPJ Web Conf. **118**, 01016 (2016), 1511.04473.  
[9] C. Aubin and T. Blum, Phys.Rev. **D75**, 114502 (2007), hep-lat/0608011.  
[10] X. Feng, K. Jansen, M. Petschlies, and D. B. Renner, Phys.Rev.Lett. **107**, 081802 (2011), 1103.4818.  
[11] P. Boyle, L. Del Debbio, E. Kerrane, and J. Zanotti,

- Phys.Rev. **D85**, 074504 (2012), 1107.1497.
- [12] M. Della Morte, B. Jager, A. Juttner, and H. Wittig, JHEP **1203**, 055 (2012), 1112.2894.
- [13] F. Burger, X. Feng, G. Hotzel, K. Jansen, M. Petschlies, and D. B. Renner (ETM), JHEP **02**, 099 (2014), 1308.4327.
- [14] B. Chakraborty et al. (HPQCD collaboration), Phys.Rev. **D89**, 114501 (2014), 1403.1778.
- [15] A. Francis, V. Guelpers, G. Herdoiza, H. Horch, B. Jaeger, H. B. Meyer, and H. Wittig, PoS **LATTICE2014**, 127 (2015), 1410.7491.
- [16] R. Malak, Z. Fodor, C. Hoelbling, L. Lellouch, A. Sastre, and K. Szabo (Budapest-Marseille-Wuppertal), PoS **LATTICE2014**, 161 (2015), 1502.02172.
- [17] E. B. Gregory and C. McNeile, PoS **LATTICE2015** (2015), 1512.00331.
- [18] M. Spraggs, P. Boyle, L. Del Debbio, A. Jttner, C. Lehner, K. Maltman, M. Marinkovic, and A. Portelli, PoS **LATTICE2015**, 106 (2016), 1601.00537.
- [19] T. Blum, M. Hayakawa, and T. Izubuchi, PoS **LATTICE2012**, 022 (2012), 1301.2607.
- [20] A. Bazavov et al. (MILC collaboration), Phys.Rev. **D82**, 074501 (2010), 1004.0342.
- [21] A. Bazavov et al. (MILC Collaboration), Phys.Rev. **D87**, 054505 (2013), 1212.4768.
- [22] R. Dowdall, C. Davies, G. Lepage, and C. McNeile (HPQCD Collaboration), Phys.Rev. **D88**, 074504 (2013), 1303.1670.
- [23] S. Borsanyi, S. Durr, Z. Fodor, C. Hoelbling, S. D. Katz, et al., JHEP **1209**, 010 (2012), 1203.4469.
- [24] B. Chakraborty, C. T. H. Davies, B. Galloway, P. Knecht, J. Koponen, G. Donald, R. Dowdall, G. Lepage, and C. McNeile, Phys. Rev. **D91**, 054508 (2015), 1408.4169.
- [25] B. Chakraborty, C. Davies, G. Donald, R. Dowdall, J. Koponen, et al. (HPQCD Collaboration), PoS **LATTICE2013**, 309 (2013), 1401.0669.
- [26] G. Donald, C. Davies, R. Dowdall, E. Follana, K. Hornbostel, et al. (HPQCD Collaboration), Phys.Rev. **D86**, 094501 (2012), 1208.2855.
- [27] B. Colquhoun, R. J. Dowdall, C. T. H. Davies, K. Hornbostel, and G. P. Lepage (HPQCD collaboration), Phys. Rev. **D91**, 074514 (2015), 1408.5768.
- [28] B. Chakraborty, C. T. H. Davies, J. Koponen, G. P. Lepage, M. J. Peardon, and S. M. Ryan, Phys. Rev. **D93**, 074509 (2016), 1512.03270.
- [29] T. Blum, P. A. Boyle, T. Izubuchi, L. Jin, A. Jttner, C. Lehner, K. Maltman, M. Marinkovic, A. Portelli, and M. Spraggs, Phys. Rev. Lett. **116**, 232002 (2016), 1512.09054.
- [30] T. Blum, Phys.Rev.Lett. **91**, 052001 (2003), hep-lat/0212018.
- [31] B. Lautrup, A. Peterman, and E. de Rafael, Phys.Rept. **3**, 193 (1972).
- [32] G. P. Lepage, in *Boulder ASI 1989:97-120* (1989), pp. 97–120, URL <http://alice.cern.ch/format/showfull?sysnb=0117836>.
- [33] A. Hart, G. von Hippel, and R. Horgan (HPQCD Collaboration), Phys.Rev. **D79**, 074008 (2009), 0812.0503.
- [34] E. Follana, Q. Mason, C. Davies, K. Hornbostel, G. P. Lepage, et al. (HPQCD and UKQCD Collaborations), Phys.Rev. **D75**, 054502 (2007), hep-lat/0610092.
- [35] E. Follana, C. Davies, G. Lepage, and J. Shigemitsu (HPQCD and UKQCD Collaborations), Phys.Rev.Lett. **100**, 062002 (2008), 0706.1726.
- [36] C. Aubin, T. Blum, P. Chau, M. Golterman, S. Peris, and C. Tu, Phys. Rev. **D93**, 054508 (2016), 1512.07555.
- [37] C. E. Wolfe and K. Maltman, Phys. Rev. **D83**, 077301 (2011), 1011.4511.
- [38] K. Hagiwara, A. D. Martin, D. Nomura, and T. Teubner, Phys. Rev. **D69**, 093003 (2004), hep-ph/0312250.
- [39] M. Ablikim et al. (BESIII), Phys. Lett. **B753**, 629 (2016), 1507.08188.
- [40] T. Aoyama, M. Hayakawa, T. Kinoshita, and M. Nio, Phys.Rev.Lett. **109**, 111808 (2012), 1205.5370.
- [41] C. Gnendiger, D. Stoeckinger, and H. Stoeckinger-Kim, Phys. Rev. **D88**, 053005 (2013), 1306.5546.
- [42] A. Kurz, T. Liu, P. Marquard, and M. Steinhauser, Phys. Lett. **B734**, 144 (2014), 1403.6400.
- [43] J. Prades, E. de Rafael, and A. Vainshtein, Adv. Ser. Direct. High Energy Phys. **20**, 303 (2009), 0901.0306.
- [44] B. Toth, **LATTICE2015** (2015).
- [45] N. Carrasco, V. Lubicz, G. Martinelli, C. T. Sachrajda, N. Tantalo, C. Tarantino, and M. Testa, Phys. Rev. **D91**, 074506 (2015), 1502.00257.
- [46] T. Blum, N. Christ, M. Hayakawa, T. Izubuchi, L. Jin, and C. Lehner, Phys. Rev. **D93**, 014503 (2016), 1510.07100.
- [47] G. Lepage, B. Clark, C. Davies, K. Hornbostel, P. Mackenzie, et al., Nucl.Phys.Proc.Suppl. **106**, 12 (2002), hep-lat/0110175.
- [48] B. Chakraborty, C. Davies, P. G. de Oliveira, J. Koponen, and G. P. Lepage, PoS **LATTICE2015**, 108 (2015), 1511.05870.
- [49] J. J. Dudek, R. G. Edwards, and C. E. Thomas (Hadron Spectrum), Phys. Rev. **D87**, 034505 (2013), [Erratum: Phys. Rev.D90,no.9,099902(2014)], 1212.0830.
- [50] J. Gasser and H. Leutwyler, Annals Phys. **158**, 142 (1984).
- [51] G. Ecker, J. Gasser, A. Pich, and E. de Rafael, Nucl. Phys. **B321**, 311 (1989).
- [52] C. Patrignani et al. (Particle Data Group), Chin. Phys. **C40**, 100001 (2016).
- [53] R. Garcia-Martin, R. Kaminski, J. R. Pelaez, J. Ruiz de Elvira, and F. J. Yndurain, Phys. Rev. **D83**, 074004 (2011), 1102.2183.
- [54] J. R. Pelaez and F. J. Yndurain, Phys. Rev. **D71**, 074016 (2005), hep-ph/0411334.
- [55] A. Bazavov et al. (MILC Collaboration), Phys.Rev. **D87**, 054505 (2013), 1212.4768.
- [56] M. Benayoun, P. David, L. DelBuono, and F. Jegerlehner (2016), 1605.04474.